IET Radar, Sonar & Navigation

Research Article

IET Journals
The Institution of Engineering and Technology

Radar cross-sections of pedestrians at automotive radar frequencies using ray tracing and point scatterer modelling

ISSN 1751-8784
Received on 3rd October 2019
Revised 28th December 2019
Accepted on 7th February 2020
E-First on 28th April 2020
doi: 10.1049/iet-rsn.2019.0471
www.ietdl.org

Yoshana Deep[1] ✉, Patrick Held[2], Shobha Sundar Ram[1], Dagmar Steinhauser[2], Anshu Gupta[3], Frank Gruson[3], Andreas Koch[3], Anirban Roy[3]

[1]*Indraprastha Institute of Information Technology Delhi, New Delhi 110020, India*
[2]*CARISSMA, Technische Hochschule Ingolstadt, Ingolstadt, Bayern, Germany*
[3]*Continental, Business Unit ADAS, UK*
✉ *E-mail: yoshana17128@iiitd.ac.in*

Abstract: Simulation of radar cross-sections of pedestrians at automotive radar frequencies forms a key tool for software verification test beds for advanced driver assistance systems. Two commonly used simulation methods are the computationally simple scattering centre model of dynamic humans and the shooting and bouncing ray technique based on geometric optics. The latter technique is more accurate but computationally complex. Hence, it is usually used only for modelling scattered returns of still human poses. In this work, the authors combine the two methods in a linear regression framework to accurately estimate the scattering coefficients or reflectivities of point scatterers in a realistic automotive radar signal model which they subsequently use to simulate range-time, Doppler-time and range-Doppler radar signatures. The simulated signatures show a normalised mean square error <10% and a structural similarity >81% with respect to measurement results generated with an automotive radar at 77 GHz.

Nomenclature

f_c	carrier frequency
γ	chirp factor
ϕ^i, ϕ^s	incident, scattering angle
θ_b	inclination of b^{th} ellipsoid
$\tau, n = 1:N$	fast time, fast time samples
$t, p = 1:P$	slow time, slow time samples
$f_s = 1/T_s$	sampling frequency
$T_{upchirp}$	up chirp duration
T_{PRI}	PRI
T_{CPI}	CPI
T_{short}	M PRIs
T_{long}	L CPIs
$1/T_f, f = 1:F$	video Frame rate, frame numbers
σ	RCS
$\epsilon' - j\epsilon''$	dielectric constant, loss tangent
$\Delta r, g = -(N/2):(N/2) - 1$	range resolution, range samples
$\Delta f_D, d = -(P/2):(P/2 - 1)$	Doppler resolution, Doppler samples
BW	radar bandwidth
x, y	continuous transmitted and received signals
$a_b, b = 1:B$	reflectivity of b^{th} scattering centre
$r_b, b = 1:B$	range of b^{th} scattering centre
$R_b, b = 1:B$	radius of b^{th} ellipsoid
$H_b, b = 1:B$	length of b^{th} ellipsoid
$\boldsymbol{\Phi}$	phase matrix based on point scatterers range
$\boldsymbol{A}$	amplitude matrix to be estimated
$\boldsymbol{\Psi}$	RCS matrix from ray tracing
$\boldsymbol{Y}$	two-dimensional radar data (fast time, slow time)
$\boldsymbol{H}_{1D}$, $\boldsymbol{H}_{2D}$	1D, 2D Window function
$\tilde{\chi}^{RD}$	simulated range-Doppler profile
$\tilde{\chi}^{RT}$	simulated range-time profile
$\tilde{\chi}^{DT}$	simulated Doppler-time profile
χ^{RT}	measured range-time profile
χ^{DT}	measured Doppler-time profile
χ^{RD}	measured range-Doppler profile

1 Introduction

Currently, ∼1.35 million road fatalities occur every year in the world [1]. Pedestrians – especially children, senior citizens and those with disabilities – are among the most vulnerable road users [2]. Recently, there has been significant research focus on developing advanced driver assistance systems (ADAS) for improving driving conditions and reducing road fatalities. Pedestrian detection, one of the key objectives of ADAS, has been researched with both automotive cameras [3, 4] and radars [5, 6]. Camera images offer key features – in the form of shapes, sizes and texture cues – for enabling automatic detection and recognition. However, the performance of the camera is affected by light and visibility conditions. Automotive radars, unlike cameras, can operate continuously, under low visibility conditions and, in some cases, in non-line-of-sight conditions as well. Radars are, however, characterised by limited angular resolution. Recently, radars have been researched for their pedestrian detection capability. The swinging motions of a pedestrian's arms and legs, while walking, give rise to distinctive Doppler radar signatures [7–9]. These micro-Doppler signals are different from those generated by other dynamic bodies on the road such as bicycles and cars and hence can be used for automatic target recognition [10–14].

The performances of these algorithms rely on the availability of large training databases gathered in a variety of scenarios. They must comprise of data from pedestrians of different ages, heights and girth; performing different activities and moving at different orientations with respect to the radar. There are two methods of generating the training data. One method is to collect the data from real pedestrians using actual automotive radar sensors. The advantage is that the training data is real and can be gathered both in laboratory conditions and during test drives. However, the disadvantage is that the database must be updated based on hardware modifications to the sensor or due to software changes in signal processing. Second, the data may be corrupted by the

presence of clutter from the local environment (both static and dynamic) and limitations of the sensor. Labelling of radar measurement data gathered over long test drives also requires painstaking efforts. Finally, pedestrians are dielectric bodies of much smaller radar cross-section (RCS) than other road targets and are unpredictable in terms of motion and posture. The alternative is to simulate the radar signatures [15–17]. The advantage is that the simulated radar signatures can be rapidly generated for a variety of sensor parameters and target scenarios. Also, the simulations can be easily integrated with the radar test bed and signal processing platforms for rapid prototyping and validations. Finally, since the simulated data may be made free of channel artifacts such as clutter, the simulation results may facilitate identifying cause and effect of the underlying radar phenomenology.

Simulations of radar micro-Doppler signatures have been extensively researched over the last decade. The animation models of human motions have included simple pendulum models of the legs [18, 19]; analytical models of constant velocity walking motion derived from bio-mechanical experiments [20]; and computer animation models for describing more complex human motions [21–25]. The motion models are subsequently combined with electromagnetic models of radar scattering off humans. Full-wave electromagnetic solvers yield very accurate predictions of RCSs. However, they are not used for modelling humans due to the considerable computational complexity (in terms of time and memory) in modelling three-dimensional (3D) spatially large dielectric bodies at automotive radar frequencies (24 and 77 GHz). Further, humans are dynamic and have a distinct pose and posture during each instant of any motion such as walking. A slightly less computationally expensive alternative is based on the shooting and bouncing rays and geometric optics and has been used for predicting the RCS of still humans at X-band and Ku-band frequencies [26–28]. However, the technique still remains computationally expensive and cannot be used to generate radar data at the pulse repetition frequencies typically used in automotive radars. Hence, ray-tracing results cannot be directly used for generating radar signatures – such as high range resolution profiles or Doppler-time spectrograms of humans – which provide key information for automatic target recognition. A third technique based on the point scattering centre model has been widely adopted for obtaining radar signatures of humans due to its low computational complexity [16, 21, 29, 30]. Here the human is modelled as an extended target with multiple point scatterers. The scattering coefficient of each point scatterer is determined from an analytical expression for RCS of a primitive shape resembling the human body part corresponding to the point scatterer. The time-varying positions of the point scatterers are obtained from computer animation data. The resulting radar signatures have shown an excellent correlation in terms of their micro-Doppler and micro-range features to the signatures derived from real measurement data. However, the method is very inaccurate in estimating the RCS magnitude due to the approximate nature of the primitive-based model and because the model does not include the effects of shadowing and multipath interactions between the different body parts. More recently, machine learning methods – specifically generative adversarial networks termed GAN – have been used to generate Doppler-time radar signatures of humans from training measurement data [31, 32]. Again, the method has been excellent in capturing the micro-Doppler features of the limb motions as opposed to the RCS values. The accurate estimation of RCS is, however, important for the implementation of radar detectors for generating receiver operating curves.

In this work, we propose a method for accurately predicting the RCS of pedestrians by combining electromagnetic ray tracing with the point scatterer model. Highly accurate estimates of RCS of the human are generated at the video frame rate using the ray-tracing technique. The reflectivities of the point scatterer human model are then estimated from the ray-tracing RCS values using linear regression. These reflectivities are subsequently integrated with the scattering centre model to generate the RCS at high radar sampling frequencies. Our method is founded on the assumption that since humans are slow moving targets, their scattering coefficients fluctuate slowly across multiple radar coherent processing intervals (CPIs) while the positions of the point scatterers change rapidly across multiple pulse repetition intervals (PRIs). The proposed method, thereby, combines the advantages of high accuracy of ray tracing with the computational performance of scattering centre modelling. We derive three types of radar signatures – high range resolution profile, Doppler-time spectrogram and range–Doppler ambiguity diagram from the simulated data. We compare the signatures with similar signatures derived from measurement radar data at 77 GHz. Our results show a low normalised mean square error (<10%) and high structural similarity (>81%) between the measured and simulated radar signatures. We also present calibrated monostatic and bistatic RCS of humans at multiple aspect angles and polarisations for both the automotive radar frequencies (24 and 77 GHz).

The paper is organised as follows. In the following section, we present the simulation methodology for hybridising the swift point scatterer modelling technique with the accurate but computationally heavy ray-tracing method. In Section 3.1 we describe the experimental set up for jointly collecting radar measurement data and motion capture (MoCap) data. We present the time-varying RCS of the human for different polarisations at 77 GHz in Section 3.2. Then, we discuss the choice of parameters used for simulating the target model in Section 3.3. Finally, we present the simulated radar signatures of the pedestrian and provide quantitative comparison with measurement results in Section 3.4. We conclude our paper in Section 4. Appendix provides additional results at 24 GHz and insights on the computational complexity.

Notation: We use the following conventions in our notations. Scalar variables are indicated by lowercase italic letters; vectors and matrices are indicated by bold italic letters.

2 Simulation methodology

The objective of the proposed work is to simulate the radar scattered signal of dynamic humans in order to generate radar signatures such as range–time, Doppler–time and range–Doppler ambiguity plots. For our method, we rely on the availability of MoCap data of a dynamic human motion at video frame rate ($1/T_f$). We begin with a stick figure animated model of human motion obtained from MoCap technology as shown in Fig. 1. Each frame of MoCap data is exported to an animation software, such as Poser Pro from Smith Micro Software [24]. Here the stick figure is embodied using one of the in-built libraries of an anatomically accurate human body. The human body is then rendered into a 3D poly-mesh figure composed of triangular facets of suitable resolution [33]. We consider the human body standing on an x - y ground plane with the height along the positive z axis. We adapted the fairly standard shooting and bouncing ray technique proposed in [34] on the poly-mesh human data for RCS estimation for different polarisations and aspect angles [26, 27]. In this technique, we consider a set of parallel, closely spaced illumination rays emanating from an incident plane at an incident angle ϕ^i. Based on the interaction between the incident rays and the mesh triangles on the human body, we compute the scattered electric field along the direction of ϕ^s. While there are several commercially available electromagnetic solvers that carry out ray tracing, we developed our solver in-house in order to customise it for speed and efficiency. The human body is a complex dielectric medium of skin, tissues and bone. However, at high frequencies (24 and 77 GHz), there is little penetration through the skin. Therefore, we model the human body as a single layer dielectric with relative permeability $\epsilon'_r(f_c) = \epsilon_r(f_c) + (\sigma_c(f_c)/j2\pi f_c\epsilon_0)$. The dielectric constant and conductivity are $\epsilon_r = 6.63$ and $\sigma_c = 38.1$ S/m at 77 GHz [35] and $\epsilon_r = 50$ and $\sigma_c = 1$ S/m at 24 GHz [26, 28]. The scattered signal strength from the human is determined by the reflection coefficient of the dielectric surface. We estimate four types of RCS. They are the co-polarised horizontal (σ^{hh}) and vertical RCS (σ^{vv}) as well as the cross-polarised RCS (σ^{hv} and σ^{vh}) at $1/T_f$. Based on the incident and scattered angles, ϕ^i and ϕ^s, we compute the bistatic RCS for different types of polarisations. When $\phi^s = \phi^i$, the RCS corresponds to the monostatic case. In the following Section 2.1, we present our proposed method to use the

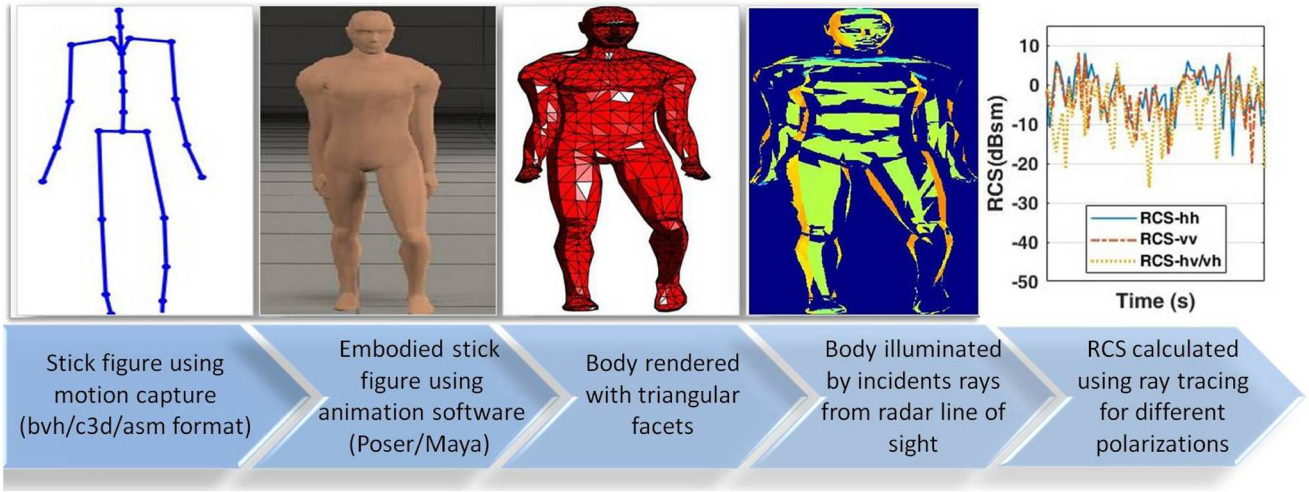

Fig. 1 *MoCap data in stick figure format is embodied using animation software like Poser/Maya. Then the body is rendered with triangular facets. Radar cross-section is calculated using electromagnetic ray tracing for different polarisations*

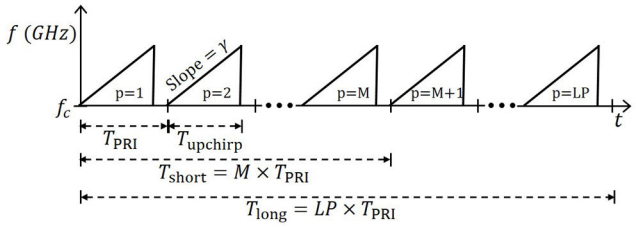

Fig. 2 *Radar signal model of linear FMCW of $T_{upchirp}$ duration with chirp rate γ and T_{PRI} PRI. Each $T_{upchirp}$ consists of N samples of $f_s = (1/T_s)$ sampling frequency. T_{long} is the duration of L CPIs each consisting of P PRIs. T_{short} is the time interval between M PRIs within T_{long}*

ray-tracing results to estimate scattering centre coefficients. Subsequently, we use these coefficients in a point scatterer model to generate scattered signals at suitable radar sampling frequencies.

2.1 Proposed method: estimation of scattering coefficients of point scatterer model using RCS from ray tracing

MoCap data describe the human posture for every frame at a video frame rate (30/48/60 Hz). The ray-tracing method provides accurate estimates of the RCS of the whole human body at each of these frames. Since the technique is computationally expensive, it cannot be used to generate radar data at high radar sampling frequencies of the order of GHz. Hence, ray-tracing results cannot be directly used for generating time-varying range–Doppler ambiguity plots of humans. In this section, we propose a method to obtain the radar signatures by hybridising the ray-tracing results and the scattering centre model using the MoCap data.

We begin by assuming that a monostatic radar is located at the origin. We model the radar transmit waveform as a frequency modulated continuous waveform (FMCW) of centre carrier frequency f_c, radar bandwidth (BW) and chirp factor $(\gamma = \mathrm{BW}/T_{\mathrm{upchirp}})$ as shown in Fig. 2. The transmit signal, $x_{\mathrm{p}}(\tau)$, over a single p$^{\mathrm{th}}$ PRI, T_{PRI}, is given by

$$x_{\mathrm{p}}(\tau) = \mathrm{rect}\left(\frac{\tau}{T_{\mathrm{PRI}}}\right) \mathrm{e}^{\mathrm{j}(2\pi f_c \tau + \pi\gamma\tau^2)}, \tag{1}$$

where

$$\mathrm{rect}\left(\frac{\tau}{T_{\mathrm{PRI}}}\right) = \begin{cases} 1, & 0 \le \tau \le T_{\mathrm{upchirp}} \\ 0, & T_{\mathrm{upchirp}} < \tau < T_{\mathrm{PRI}} \end{cases}. \tag{2}$$

The interval between the up chirp duration T_{upchirp} and T_{PRI} may be regarded as dead time. We assume that the transmitted waveform spans T_{long} duration consisting of L CPIs each of P PRIs. The radar signal falls upon a dynamic target of B point scatterers with scattering coefficients or reflectivities, $\{a_b, b = 1{:}B\}$. These are assumed to be constant over the radar bandwidth and over the duration of T_{long}. If the time-varying radial distance of each b$^{\mathrm{th}}$ point scatterer with respect to the radar is $r_b(t)$, then the approximate baseband received signal can be written as

$$y(\tau, t) \simeq \sum_{b=1}^{B} a_b \mathrm{rect}\left(\frac{\tau - (2r_b(t)/c)}{T_{\mathrm{PRI}}}\right) \exp\left(-\mathrm{j}2\pi f_c \frac{2r_b(t)}{c}\right) \exp\left(\mathrm{j}\pi\gamma\left(\tau - \frac{2r_b(t)}{c}\right)^2\right), \tag{3}$$

where c is the velocity of the light. The model in (3) is called the primitive model or scattering centre model. This model is computationally simple to use to generate radar signatures, provided the positions and scattering coefficients of the scattering centres are available. Generally, the scattering centres are assumed to correspond to trackers placed on the live subject whose positions are gathered using MoCap technology. The position vector data ($\boldsymbol{r}_b$) of B scatterers are spline interpolated from $1/T_{\mathrm{f}}$ to the pulse repetition frequency ($1/T_{\mathrm{PRI}}$) of the radar. In prior works, a_b, of the B scatterers have been estimated from the size, shape and orientation of primitives of body parts corresponding to the scattering centres [20, 30]. For example, a marker placed on the human arm corresponds to an ellipsoid of dimensions comparable to the human arm. The approximate nature of the estimation of a_b results in very poor accuracy in the magnitude of the radar signatures. We propose to use the ray-tracing results to obtain more accurate estimates of the scattering coefficients.

The n$^{\mathrm{th}}$ fast time sample of the discrete received signal for the p$^{\mathrm{th}}$ PRI is

$$\boldsymbol{Y}[nT_{\mathrm{s}}, pT_{\mathrm{PRI}}] = \boldsymbol{Y}[n, p] = \sum_{b=1}^{B} a_b \mathrm{rect}\left(\frac{n - (2r_b[p]/cT_{\mathrm{s}})}{N}\right) \exp\left(-\mathrm{j}2\pi f_c \frac{2r_b[p]}{c}\right) \exp\left(\mathrm{j}\pi\gamma\left(nT_{\mathrm{s}} - \frac{2r_b[p]}{c}\right)^2\right). \tag{4}$$

Here $\{p = 1{:}LP\}$ correspond to the PRIs within L CPIs while $\{n = 1{:}N\}$ corresponds to the fast time samples within one PRI as shown in Fig. 2. Ray-tracing techniques provide the RCS estimates $(\sigma^{\mathrm{vv}}[fT_{\mathrm{f}}], \sigma^{\mathrm{hh}}[fT_{\mathrm{f}}])$ for the whole human body at the video frame rate of the MoCap data. Since automotive radars usually use vertically polarised waveforms, we interpolate $\sigma^{\mathrm{vv}}[f], f = 1{:}F$ to radar pulse repetition frequency to get $\sigma^{\mathrm{vv}}[p], p = 1{:}P$. The scattering coefficients are assumed to be uniform across the radar bandwidth at automotive radar frequencies. Therefore, $\sqrt{\sigma^{\mathrm{vv}}[p]}$

may be regarded as the first fast time sample of the scattered signal in (4), of every p$^{\text{th}}$ PRI with $\gamma = 0$

$$\sqrt{\sigma^{\text{vv}}[p]} = \boldsymbol{Y}[n=1,p] = \sum_{b=1}^{B} a_b \exp\left(-\text{j}2\pi f_{\text{c}} \frac{2r_b[p]}{c}\right). \tag{5}$$

Since humans move slowly, a_b fluctuates very slowly across L CPIs (T_{long}) but $\boldsymbol{r}_b$ changes significantly across M PRIs ($T_{\text{short}} = M \times T_{\text{PRI}}$). Therefore, we can frame a linear regression model $\boldsymbol{\Phi A} = \boldsymbol{\Psi}$ using

$$\boldsymbol{\Phi} = \begin{bmatrix} \text{e}^{-\text{j}2\pi f_{\text{c}}(2r_1[1]/c)} & \dots & \text{e}^{-\text{j}2\pi f_{\text{c}}(2r_B[1]/c)} \\ \text{e}^{-\text{j}2\pi f_{\text{c}}(2r_1[M]/c)} & \dots & \text{e}^{-\text{j}2\pi f_{\text{c}}(2r_B[M]/c)} \\ \vdots & \ddots & \vdots \\ \text{e}^{-\text{j}2\pi f_{\text{c}}(2r_1[LP]/c)} & \dots & \text{e}^{-\text{j}2\pi f_{\text{c}}(2r_B[LP]/c)} \end{bmatrix} \tag{6}$$

and

$$\boldsymbol{A} = \begin{bmatrix} a_1 \\ a_2 \\ \vdots \\ a_B \end{bmatrix}, \quad \boldsymbol{\Psi} = \begin{bmatrix} \sqrt{\sigma^{\text{vv}}[1]} \\ \sqrt{\sigma^{\text{vv}}[M]} \\ \vdots \\ \sqrt{\sigma^{\text{vv}}[LP]} \end{bmatrix}. \tag{7}$$

The integer number of rows of $\boldsymbol{\Phi} \in \mathbb{C}^{K \times B}$ is obtained by rounding $\lfloor LP/M \rfloor$ to the nearest integer. We estimate the reflectivities of the B point scatterers by solving for $\boldsymbol{A}$ using ordinary least squares ($\min_{\boldsymbol{A}} \parallel \boldsymbol{\Psi} - \boldsymbol{\Phi A} \parallel_2^2$) [36], as shown below

$$\boldsymbol{A} = \left(\boldsymbol{\Phi}^{\text{T}}\boldsymbol{\Phi}\right)^{-1}\boldsymbol{\Phi}^{\text{T}}\boldsymbol{\Psi}. \tag{8}$$

Once the scattering centre coefficients are estimated, they can be used in (4) to obtain the radar received data $\boldsymbol{Y}[n,p]$. The choices of L (and thereby T_{long}) as well as M (and T_{short}) are critical while P is fixed by the radar specifications. Since humans are typically slow moving targets, low values of T_{short} will result in very small changes between $r_b[p]$ and $r_b[p+M]$. This could result in singularity errors in the solution. On the other hand, large values of T_{short} will result in large T_{long} intervals which is undesirable since the scattering coefficients are unlikely to remain unchanged over long durations.

In the above method, we have discussed how to estimate a_b for a monostatic radar configuration of vertically polarised radar. However, the method can be easily modified to allow considerable flexibility in terms of the radar carrier frequency, bandwidth, radar position, aspect angles and polarisation.

- Depending on the polarisation requirement of the simulation framework, we can generate radar data by selecting corresponding RCS values ($\sigma^{\text{vv}}, \sigma^{\text{hh}}, \sigma^{\text{vh}}$ and σ^{hv}) computed from ray tracing for $\boldsymbol{\Psi}$ in (6).
- Similarly, we can change from monostatic to bistatic radar configuration in (3). We can obtain the bistatic radar signatures by choosing the bistatic RCS values computed from ray tracing.

2.2 Generation of radar signatures

The 2D radar data $\boldsymbol{Y}[n,p]$ along the fast and slow time axes are processed through Fourier transform to obtain three types of radar signatures for every T_{long} duration. The three signatures are: range–time ($\tilde{\chi}^{\text{RT}}$), Doppler–time ($\tilde{\chi}^{\text{DT}}$) and time-varying range–Doppler ambiguity plots ($\tilde{\chi}^{\text{RD}}$). As mentioned earlier, each T_{long} interval of the radar data consists of L CPIs, where each CPI is of P PRIs.

The range-time profile is generated by implementing the 1D Fourier transform on $\boldsymbol{Y}[n,p]$ along the fast time axis for each p$^{\text{th}}$ PRI as shown in

$$\begin{aligned} \tilde{\chi}_{\text{p}}^{\text{RT}}[g\Delta r] = \tilde{\chi}_{\text{p}}^{\text{RT}}[g] &= \sum_{n=1}^{N} \boldsymbol{Y}[n,p]\boldsymbol{H}_{\text{1D}}[n]\,\text{e}^{-\text{j}(2\pi gn/N)}, \\ g &= \frac{-N}{2} : \frac{N}{2} - 1. \end{aligned} \tag{9}$$

Here, $\Delta r = (c/2\text{BW})$ is the range resolution and $\boldsymbol{H}_{\text{1D}}[\,\cdot\,] \in \mathbb{R}^{N\times 1}$ is a 1D window function.

The Doppler velocity spectrogram is generated by implementing the 1D Fourier transform on $\boldsymbol{Y}[n=1,p]$ along the slow time axis for each l$^{\text{th}}$ CPI as shown in

$$\begin{aligned} \tilde{\chi}_{l}^{\text{DT}}[d\Delta f_{\text{D}}] &= \tilde{\chi}_{l}^{\text{DT}}[d] \\ &= \sum_{p=(l-1)P+1}^{lP} \boldsymbol{Y}[n=1,p]\boldsymbol{H}_{\text{1D}}[p]\text{e}^{-\text{j}(2\pi dp/P)}, \\ d &= \frac{-P}{2} : \frac{P}{2} - 1. \end{aligned} \tag{10}$$

Here, $\Delta f_{\text{D}} = (1/PT_{\text{PRI}})$ is the Doppler resolution.

Range–Doppler ambiguity plots are generated for each l$^{\text{th}}$ CPI through 2D Fourier transform of $\boldsymbol{Y}[n,p]$ along the fast and slow time axes as shown below

$$\begin{aligned} \tilde{\chi}_{l}^{\text{RD}}[g,d] = &\sum_{p=(l-1)P+1}^{lP} \sum_{n=1}^{N} \boldsymbol{Y}[n,p]\boldsymbol{H}_{\text{2D}}[n,p]\,\text{e}^{-\text{j}(2\pi gn/N)} \\ &\text{e}^{-\text{j}(2\pi dp/P)}. \end{aligned} \tag{11}$$

Here, $\boldsymbol{H}_{\text{2D}}[\,\cdot\,] \in \mathbb{R}^{N\times P}$ is a 2D window function. The process is repeated across all the L CPIs to obtain the time-varying range–Doppler ambiguity plots. Algorithm 1 (see Fig. 3) summarises the proposed simulation methodology to generate the radar signatures with accurate scattering centre coefficients for every T_{long} period.

3 Experimental results

In this section, we present the experimental results for validating the proposed methodology. We collect MoCap data of human motion and use it to simulate radar data. Simultaneously, we collect hardware-based radar data for the same human subject from a measurement setup at 77 GHz. We perform ray tracing on the 3D poly-mesh structure obtained from the stick figure animation of every frame of the MoCap data to simulate the monostatic RCS of the pedestrian for vertical polarisation. Then we use these values to generate scattering coefficients of the scattering centre model of a human. Finally, we generate the simulated radar signatures which we compare with measurement results.

3.1 Experimental data collection

We present the experimental setup in this section. We consider a human subject moving along the trajectory shown in Fig. 4. We collect MoCap data of the human motion using Xsens MTw Awinda [37], an inertial measurement unit containing 3D linear accelerometers and rate gyroscopes. 17 trackers are attached to defined locations on the front and back of the subject's body to measure the motion of each body segment. Additionally, position information of six other body segments on the torso and feet are determined by interpolation by the MoCap software. Wireless communication between the sensors and the synchronisation station takes place at 60 Hz frame rate. The MoCap data of the 23 markers are used for simulating the radar returns. For validation purposes, the radar returns from the subject are simultaneously captured using a 77 GHz linear frequency-modulated INRAS RadarLog sensor [7, 38]. The simulation parameters for the radar signal model discussed in Section 2.1 are chosen to match the radar hardware configurations as listed in Table 1.

Input: MoCap data of B point scatterers on the human body at video frame rate ($\frac{1}{T_f}$): $\{\boldsymbol{r}_b[fT_f] = \boldsymbol{r}_b[f],\ b = 1 : B\}$

1. Implement ray tracing on three-dimensional poly-mesh structure obtained from stick figure for every frame $\sigma^{\text{vv}}[f], f = 1 : F$
2. Spline interpolate frames $\{f = 1 : F\}$ of position vector of point scatterer data along with the RCS derived from ray tracing from video frame rate to radar pulse repetition frequency ($\frac{1}{T_{\text{PRI}}}$) to obtain $\{p = 1 : LP\}$ values.
(i) $\boldsymbol{r}_b[f] \longrightarrow \boldsymbol{r}_b[p]$
(ii) $\sigma^{\text{vv}}[f] \longrightarrow \sigma^{\text{vv}}[p]$
3. Formulate $\boldsymbol{\Phi} \in \mathbb{C}^{K \times B}$ where $K = \lfloor \frac{LP}{M} \rfloor \approx B$ such that

$$\boldsymbol{\Phi} = \begin{bmatrix} e^{-j2\pi f_c \frac{2r_1[1]}{c}} & \dots & e^{-j2\pi f_c \frac{2r_B[1]}{c}} \\ e^{-j2\pi f_c \frac{2r_1[M]}{c}} & \dots & e^{-j2\pi f_c \frac{2r_B[M]}{c}} \\ \vdots & \ddots & \vdots \\ e^{-j2\pi f_c \frac{2r_1[LP]}{c}} & \dots & e^{-j2\pi f_c \frac{2r_B[LP]}{c}} \end{bmatrix}.$$

Also formulate

$$\boldsymbol{A} = \begin{bmatrix} a_1 \\ a_2 \\ \vdots \\ a_B \end{bmatrix}, \boldsymbol{\Psi} = \begin{bmatrix} \sqrt{\sigma^{\text{vv}}[1]} \\ \sqrt{\sigma^{\text{vv}}[M]} \\ \vdots \\ \sqrt{\sigma^{\text{vv}}[LP]} \end{bmatrix}.$$

4. Estimate the reflectivities of B point scatterers by $\boldsymbol{A} = \left(\boldsymbol{\Phi}^T\boldsymbol{\Phi}\right)^{-1}\boldsymbol{\Phi}^T\boldsymbol{\Psi}$ using ordinary least squares minimization of $||\boldsymbol{\Psi} - \boldsymbol{\Phi}\boldsymbol{A}||_2^2$.
5. **Output:** Model received radar signal using position and estimated reflectivities of point scatterers for every n^{th} fast time sample of p^{th} PRI.

$$\boldsymbol{Y}[n,p] = \sum_{b=1}^{B} a_b \,\text{rect}\left(\frac{n - \frac{2\boldsymbol{r}_b[p]}{cT_s}}{N}\right) \exp\left(-j2\pi f_c \frac{2\boldsymbol{r}_b[p]}{c}\right) \exp\left(j\pi\gamma\left(nT_s - \frac{2\boldsymbol{r}_b[p]}{c}\right)^2\right).$$

6. Use $\boldsymbol{Y}[n,p]$ to obtain three types of radar signatures:
- Implement 1D Fourier transform on $\boldsymbol{Y}[n,p]$ along fast time axis (n) for every p^{th} PRI to obtain radar range-time signature ($\tilde{\boldsymbol{\chi}}^{\text{RT}}$).
- Implement 1D Fourier transform on $\boldsymbol{Y}[n,p]$ along slow time axis (p) for every CPI (P PRIs) to obtain Doppler-time spectrogram ($\tilde{\boldsymbol{\chi}}^{\text{DT}}$).
- Implement 2D Fourier transform on $\boldsymbol{Y}[n,p]$ to obtain range-Doppler ambiguity plot ($\tilde{\boldsymbol{\chi}}^{\text{RD}}$).

Fig. 3 *Algorithm 1: Simulation of radar signatures for every $T_{long} = LP\,T_{PRI}$*

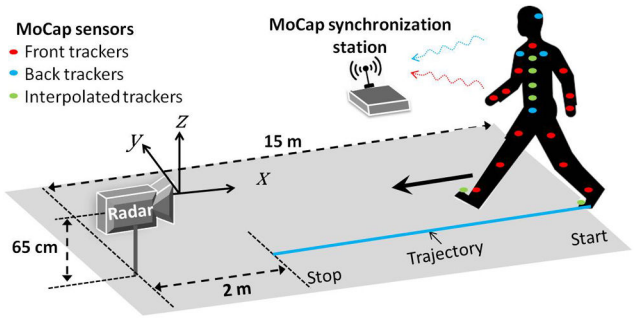

Fig. 4 *Subject wearing 17 trackers in front (red) and back (blue) view; six interpolated trackers (green), for collecting MoCap data, walks radially towards the radar sensor (INSAR RadarLog) from 15 m distance and stops 2 m before the radar along the trajectory (indicated by blue line). The radar sensor is positioned at [0, 0, 0.65] m. The wireless communication between the MoCap sensors and the synchronisation station takes place at 60 Hz frame rate*

3.2 Results from electromagnetic ray tracing

The animated stick figure model obtained from MoCap is embodied using an in-built library of a nude male in Poser Pro software from Smith Micro Inc. [24]. Each frame of the human body is subsequently rendered into a 3D poly-mesh structure composed of 3052 triangular facets. The data for each frame consists of 3D position coordinates of the triangle's vertices which are exported to MATLAB for further processing. The simulations are performed for both co-polarisation and cross-polarisation scenarios. Based on the scattered signal from all the body parts, we estimate the total monostatic RCS of the human at every frame of the MoCap data. We present the results for a complete walking stride – the full swing motion of a hand/leg – of 69 frames from 2.8 to 3.9 s in Fig. 5 for different incident aspect angles. The figure shows that the co-polarisation (σ^{vv} and σ^{hh}) components range from −10 to +5 dBsm. The cross-polarisation components are generally weaker by ∼10 dB. These RCS values are within the range of those reported from measurement studies of pedestrians at X-band frequencies [28, 39]. The versatility of the ray-tracing methodology allows us to compute RCS at a variety of radar configurations including carrier frequencies, polarisations and radar positions. In Section 6.1 of Appendix, we present the monostatic radar RCS at 24 GHz, the other popular automotive radar frequency. We also provide the bistatic RCS values at both 24 and 77 GHz.

All the results presented in this section were generated with ray tracing alone. The next set of results are generated by hybridisation of ray tracing and point scatterer modelling. We use the vertical co-polarised RCS (σ^{vv}) values at front incidence $\left(\phi^{\text{i}} = 0°\right)$ to match the radar hardware configurations.

3.3 Discussion on parameters

The scattering coefficients are estimated by solving the linear regression framework in (5). Here T_{long} (and L) and T_{short} (and M) are carefully chosen while P is fixed according to the radar's PRI. Both L and M determine K, the number of rows in $\boldsymbol{\Phi}$ matrix, since K is rounded to the nearest integer $\lfloor LP/M \rfloor$. Fig. 6*a* shows the average l_2 norm error, $\| \boldsymbol{\Psi} - \boldsymbol{\Phi}\boldsymbol{A} \|_2^2 / \| \boldsymbol{\Psi} \|_2^2$ for different values of K. When K is very large due to small values of M, we get very high errors. This is because, for slow moving targets, such as humans, there is a very small variation in the position of some of the scatterers (such as torso) in consecutive T_{short} intervals. This results in singularities in the problem formulation. We find that the optimum results occur when $K \simeq B$, that is when the $\boldsymbol{\Phi}$ matrix is close to a square matrix. Different combinations of L and M can result in similar values of K. However, when M is very large, this gives rise to a correspondingly large value of $L = (MK/P)$. However, long T_{long} duration is undesirable since scattering coefficients are likely to fluctuate over long intervals due to variations in target aspect. We compared the NMSE of the measured and simulated range–time ambiguity plots for different M for a fixed $K = 23(= B)$ and $K = 26$ in Fig. 6*b*. The result shows that the NMSE is lowest for a slightly over-determined matrix when $K = 26(= B + 3)$. Based on the above studies, we determined $M = 80$ and $L = 2$ to be the optimum values for our simulation.

3.4 Radar signatures generated from simulated and measured radar data

Based on the choice of M and L, the T_{long} and T_{short} used in the linear regression framework are 12.5 and 4.9 ms, respectively. We present three types of radar signatures: the high range resolution profile, the Doppler-time spectrogram and the range–Doppler ambiguity plots. We compare these signatures with those generated from other simulation methods and from measurement data collected from the radar hardware.

Currently, the most commonly used method to simulate radar signatures of dynamic humans is the primitive-based modelling as described originally in [29] and then used widely in literature [23, 30, 40]. In this technique, the different body parts are modelled as

Table 1 Radar parameters used for simulation are chosen to match the INRAS RadarLog sensor

Parameters	Values
carrier frequency (f_c)	77 GHz
bandwidth (BW)	2 GHz
sampling frequency (f_s)	10 MHz
up chirp duration ($T_{upchirp}$)	51.2 μs
PRI (T_{PRI})	61.2 μs
no. of chirps per CPI (P)	1024
range resolution (Δr)	7.5 cm
Doppler resolution (Δf_D)	15.9 Hz
radar sensor position	[0, 0, 0.65] m

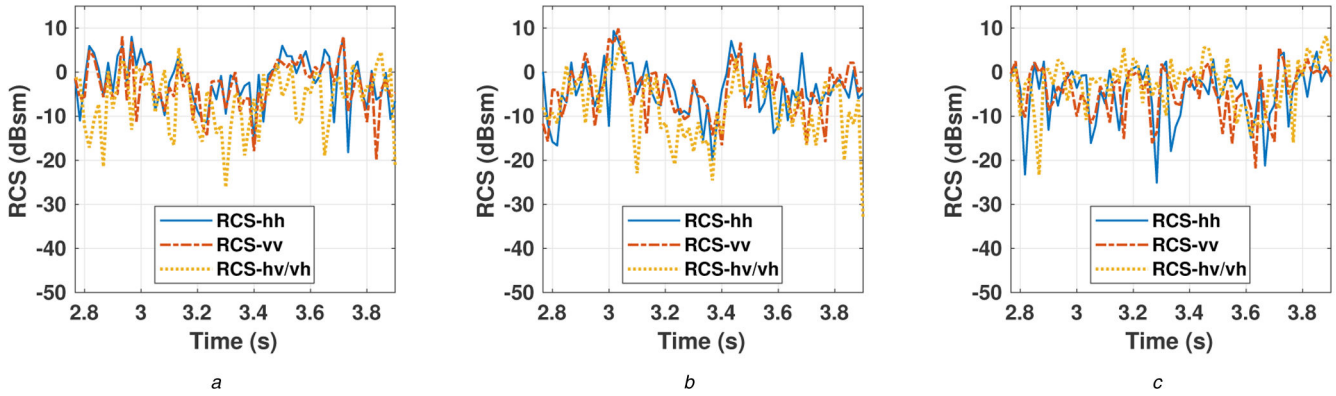

Fig. 5 *Simulated monostatic ($\phi^i = \phi^s$) RCS across multiple frames corresponding to one walking stride obtained from ray tracing at 77 GHz for three aspect angles*

(a) Front incidence ($\phi^i = 0°$), ***(b)*** Oblique incidence ($\phi^i = 45°$) and, ***(c)*** 90° incidence ($\phi^i = 90°$)

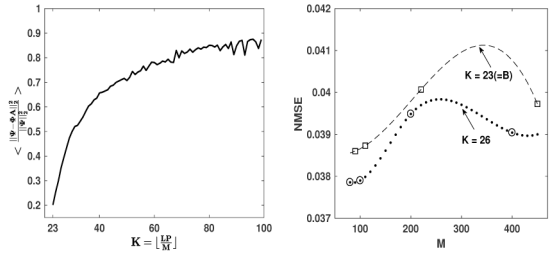

Fig. 6 *To make the choice of T_{long} (and L) and T_{short} (and M)*

(a) Estimation error $\| \boldsymbol{\Psi} - \boldsymbol{\Phi A} \|_2^2 / \| \boldsymbol{\Psi} \|_2^2$ averaged over the number of estimations done for the duration of target motion for different values of $K = \lfloor LP/M \rfloor$ is plotted, ***(b)*** Comparing the NMSE between simulated and measured range–time plots for $K = 23$ and $K = 26$ for different values of M

dielectric ellipsoids whose dimensions are chosen to closely resemble that of the test subject. We list the dimensions of the ellipsoidal body parts, which we used in this paper, in Table 2. The RCS of an ellipsoid [41] of length H_b and radius R_b, at high frequencies, is

$$\sigma_b = \left[\frac{(1/4)\pi^2 R_b^4 H_b^2}{R_b^2 \sin^2\theta_b + (1/4) H_b^2 \cos^2\theta_b} \right]^{1/2}, \tag{12}$$

where θ_b is the angle between the incident vector from the radar and the height axis of the ellipsoid. The strength of the scattered signal from the bth part of the extended target, a_b, depends on the material properties, dimensions and the aspect angle ($a_b = \Gamma(\theta_b[n])\sqrt{\sigma_b[n]}$). We incorporate the dielectric material properties of the target into the RCS estimation through Fresnel reflection coefficient, $\Gamma(\theta_b)$, for planar interfaces.

The measurement data is suitably range compensated to obtain the time-varying RCS of the target. Since this data is naturally corrupted by noise, an ordered statistics constant false alarm rate algorithm based on [42] is implemented on the measurement data. The algorithm adaptively estimates the detection threshold for each cell based on neighbouring cells. The CFAR algorithm is not required on the simulation data where noise is not considered. We present both qualitative and quantitative comparisons between the simulated and measured radar signatures.

First, we present the high range resolution profile of the walking human in Fig. 7*a* (proposed), Fig. 8*a* (primitive) and Fig. 9*a* (measured). The first two figures are generated from simulation data ($\tilde{\chi}^{RT}$) while the third is from measurement data (χ^{RT}). Values <−40 dBsm threshold are not shown in all of the figures. We observe that the human is the first stationary for 1.5 s and then approaches the radar from a range of 15–2 m from 1.5 to 10.3 s. The swinging motion of the arms and legs give rise to micro-range features about the torso that spans ∼1.5 m. The range ambiguity is 7 cm. Therefore, it is difficult to resolve the independent point scatterers from the different body parts along the range. The simulated results from the proposed technique closely resemble the measured results in terms of dynamic range. The torso appears to be the strongest component in both images when compared to the arms and legs. The range spread due to the spatial extent of the target is nearly identical in both the images (indicated by horizontal-dashed lines). The vertical-dashed lines in both figures indicate the similarity in time span also. Thus visually, there is a structural similarity in the images. The result from the primitive-based figure shows many similar features to the measurement results with respect to the micro-range characteristics. However, the strength appears much weaker.

Next, we examine the Doppler-spectrograms from the simulated data ($\tilde{\chi}^{DT}$) in Figs. 7*b* and 8*b* and measured data (χ^{DT}) in Fig. 9*b*. Since the human is approaching the radar, the Dopplers are mostly positive with some negative Dopplers due to the back swing of the arms and legs. The human is walking at a velocity of ∼1.5 m/s. This results in a strong torso Doppler component in both Figs. 7*b* and 9*b*. We can observe much weaker micro-Dopplers from the arms and legs up to velocities of 5 m/s. The Doppler span for measurement results is slightly higher than the simulated results due to noise characteristics. The periodicity of the strides in all

Table 2 Dimensions of ellipsoids used to model different body parts. Parameters that were chosen to match the test subject's body dimensions

Body parts	Radius (R_b), cm	Length (H_b), cm	Body parts	Radius (R_b), cm	Length (H_b), cm
pelvis	18.14	10.25	left shoulder	4.1	14.7
lower back	15.7	11.3	left upper arm	3.51	30.5
upper back	14.3	10.2	left lower arm	2	25
lower torso	16.3	31.7	right upper thigh	7.8	8.3
upper torso	15.24	10.2	right upper leg	4.6	47
neck	5.64	9.5	right lower leg	3.5	41.1
head	8.1	14.3	right foot	2	18.2
right collar	10	8.6	left upper thigh	7.77	8.3
right shoulder	4.11	14.7	left upper leg	4.6	47
right upper arm	3.51	30.5	left lower leg	3.5	41.1
right lower arm	2	25	left foot	2	18.2
left collar	10	8.6	—	—	—

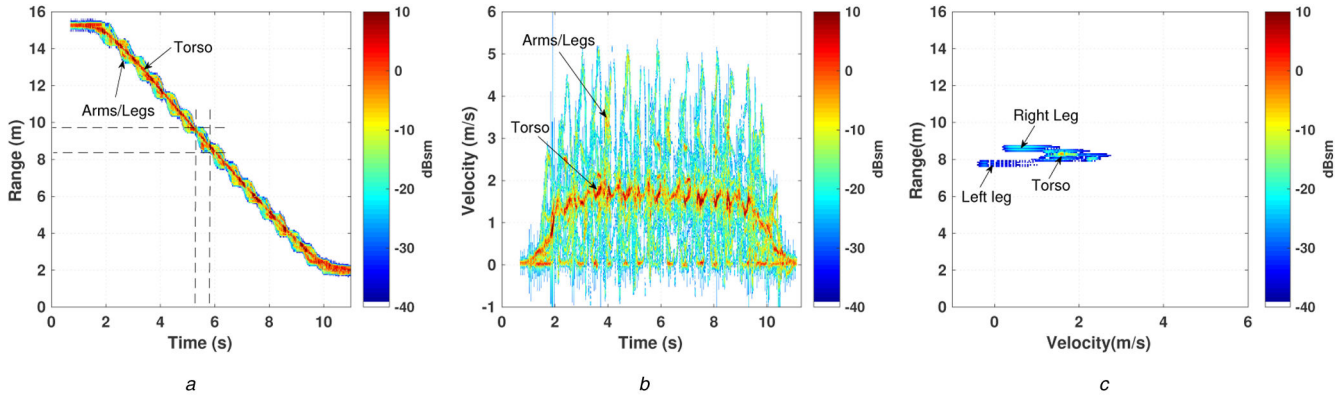

Fig. 7 *Simulated radar signatures of a human walking towards a 77 GHz monostatic radar using the proposed hybrid of primitive modelling and ray tracing*
(a) Range–time ambiguity plot, ***(b)*** Doppler–time ambiguity plot, ***(c)*** Range–Doppler ambiguity plot for one CPI (from 6.16 to 6.22 s)

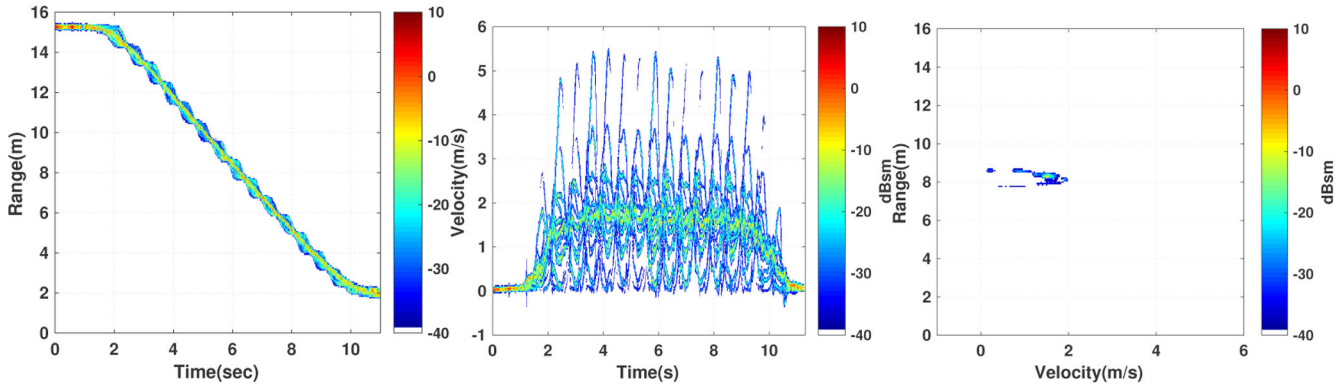

Fig. 8 *Simulated radar signatures of a human walking towards a 77 GHz monostatic radar using primitive modelling*
(a) Range–time ambiguity plot, ***(b)*** Doppler–time ambiguity plot, ***(c)*** Range–Doppler ambiguity plot for one CPI (from 6.16 to 6.22 s)

three figures shows excellent agreement. There is a strong DC component in the simulation figures that is not present in the measurement results due to a DC filter in the radar hardware to eliminate static clutter. Again, the strength of the RCS is significantly weaker in the simulated results obtained from primitive modelling in Fig. 8*b*.

Finally, we present the range–Doppler ambiguity plot for a single CPI (from 6.16 to 6.22 s) in Figs. 7*c*, 8*c* and 9*c*. Here we observe that the range and Doppler ambiguities in the simulated image from the proposed method ($\tilde{\chi}^{\mathrm{RD}}$) and measured data ($\chi^{\mathrm{RD}}$) are nearly identical. We are now able to resolve the arms, legs and torso in the ambiguity plots. The simulation result enables us to correctly identify the different body parts. Again the peak and dynamic range of the two plots are very similar while the dynamic range of Fig. 8*c* is weaker and the legs and arms are not easily observed.

In the above discussion, we have qualitatively compared the simulated and measured results. Next, we perform a quantitative comparison between the two signatures. There are a plethora of metrics in the image processing literature for comparing RGB values in the pixels of different images. However, not all of these are suited for comparing the signal strength in the bins in radar ambiguity plots. In our paper, we have selected four metrics – the normalised mean square error (NMSE), the structural similarity index (SSIM), the normalised cross-correlation (NCC) and mutual information (MI) – for comparing simulated and measured radar images. The NMSE for the range time plot is computed by

$$\mathrm{NMSE} = \frac{\| \tilde{\chi}^{\mathrm{RT}} - \chi^{\mathrm{RT}} \|_2^2}{\| \chi^{\mathrm{RT}} \|_2^2}. \tag{13}$$

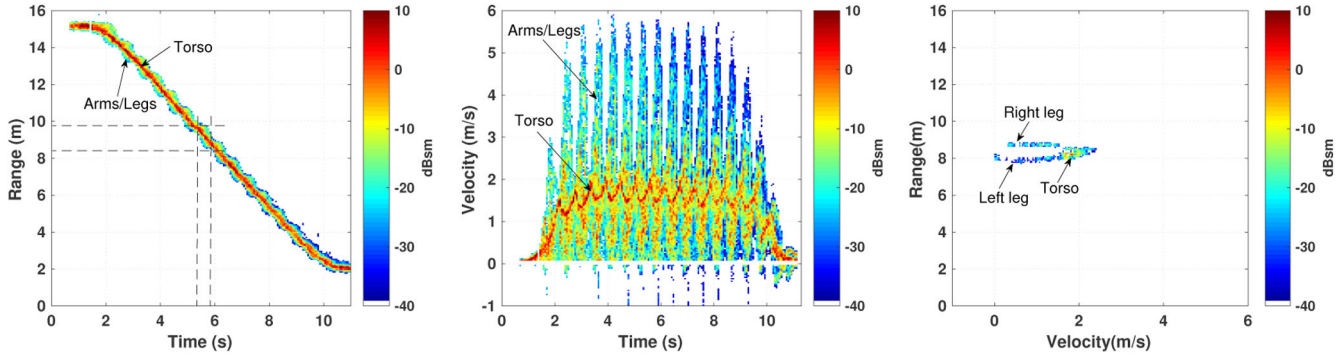

a *b* *c*

Fig. 9 *Measured radar signatures of a human walking towards a 77 GHz monostatic radar*
(a) Range–time ambiguity plot, ***(b)*** Doppler–time ambiguity plot, ***(c)*** Range–Doppler ambiguity plot for one CPI (from 6.16 to 6.22 s)

Table 3 Quantitative comparison between simulated and measured range-time, Doppler time and range-Doppler plots for first target trajectory

Algorithm	Metric	Range versus time	Doppler versus time	Range versus Doppler
proposed	SSIM	0.86	0.81	0.99
proposed	NMSE	0.04	0.10	0.03
proposed	NCC	0.99	1.0	0.98
proposed	MI	0.28	0.33	0.02
primitive	SSIM	0.0017	3×10^{-4}	6×10^{-4}
primitive	NMSE	0.3	0.69	0.22
primitive	NCC	0.97	0.98	0.98
primitive	MI	0.22	0.03	0.01

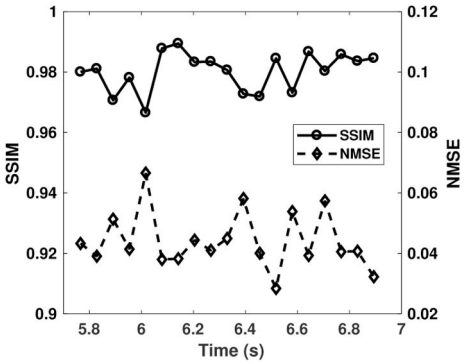

Fig. 10 *SSIM and NMSE values for range–Doppler plots for one complete walking stride from 5.76 to 6.89 s*

The SSIM is a metric used for comparing structural differences such as luminance and contrast between two images [43]. It is computed by

$$\mathrm{SSIM} = \frac{(2E[\tilde{\chi}]E[\chi])(2\mathrm{covar}[\tilde{\chi}, \chi])}{(E^2[\tilde{\chi}] + E^2[\chi])(\mathrm{var}[\tilde{\chi}] + \mathrm{var}[\chi])}, \tag{14}$$

where $E[\cdot]$, $\mathrm{var}[\cdot]$ and $\mathrm{covar}[\cdot]$ denote mean, variance and covariance of the two images. When the images are identical, its value is 1. The NCC between two images is computed by

$$\mathrm{NCC} = \frac{\| \chi^{\mathrm{RT}} \circ \tilde{\chi}^{\mathrm{RT}} \|_2^2}{\| \chi^{\mathrm{RT}} \|_2^2 \, \| \tilde{\chi}^{\mathrm{RT}} \|_2^2} \tag{15}$$

where $\circ$ indicates a Hadamard product between two matrices. MI between two images is computed by

$$\mathrm{MI} = \sum_{x \in \chi^{\mathrm{RT}}} \sum_{y \in \tilde{\chi}^{\mathrm{RT}}} p(x, y) \log\left(\frac{p(x, y)}{p(x)p(y)}\right), \tag{16}$$

where $p(\cdot)$ indicates the frequency of occurrence of the pixel value ($x \in \chi^{\mathrm{RT}}$ or $y \in \tilde{\chi}^{\mathrm{RT}}$) in the images. Table 3 shows the four metrics for the three radar signatures for the duration of the target motion. The images generated from the two types of simulation methods – proposed and primitive – are compared with the measurement results. In the case of the proposed method, all three signatures show low values of NMSE and SSIM values close to 1 which indicates the close similarity between the simulation and measurement data. Fig. 10 shows the NMSE and the SSIM between the simulated and measured range–Doppler ambiguity plots over the duration of one walking stride (9 T_{long}) from 5.76 to 6.89 s. The results in the figure show the range of SSIM between 0.96 and 0.99 which is close to ideal. The NMSE is likewise close to zero. When we compare these values to those obtained for the primitive-based modelling, the differences are stark. Due to the poor estimation of the RCS strength by the primitive-based method, the NMSE is high and the SSIM is low. Next, we consider the NCC for the two methods. Here, we observe that the NCC is close to 1 for all three signatures for both the proposed and primitive-based simulation methods. This high value is because the NCC shows the correspondence of the micro-range and micro-Doppler features between the simulated and measured results and not necessarily with the strength of the radar returns. Finally, when we consider MI, we observe that the MI is higher for the proposed method when compared to the primitive-based method for all three signatures. The metric is, however, not very intuitive compared to the previous three metrics that were discussed.

We have considered a second scenario where a human is initially still during the first 1.5 s. Then he walks away from the radar and then turns and walks across the radar as shown in Fig. 11*a*. Again, we simulated the range-time and Doppler-time radar RCS signatures using the proposed method and validated the results with the measurement data. Note that since the results are presented in terms of RCS, their maximum and minimum values are nearly identical to the results obtained for the previous trajectory. This is because the RCS is generated for the same human subject and is independent of the distance of the target with respect to the radar. The Doppler-time measurement results in Fig. 11*b* shows that the Dopplers are initially negative when the subject moves away from the radar. Here, we can see the micro-

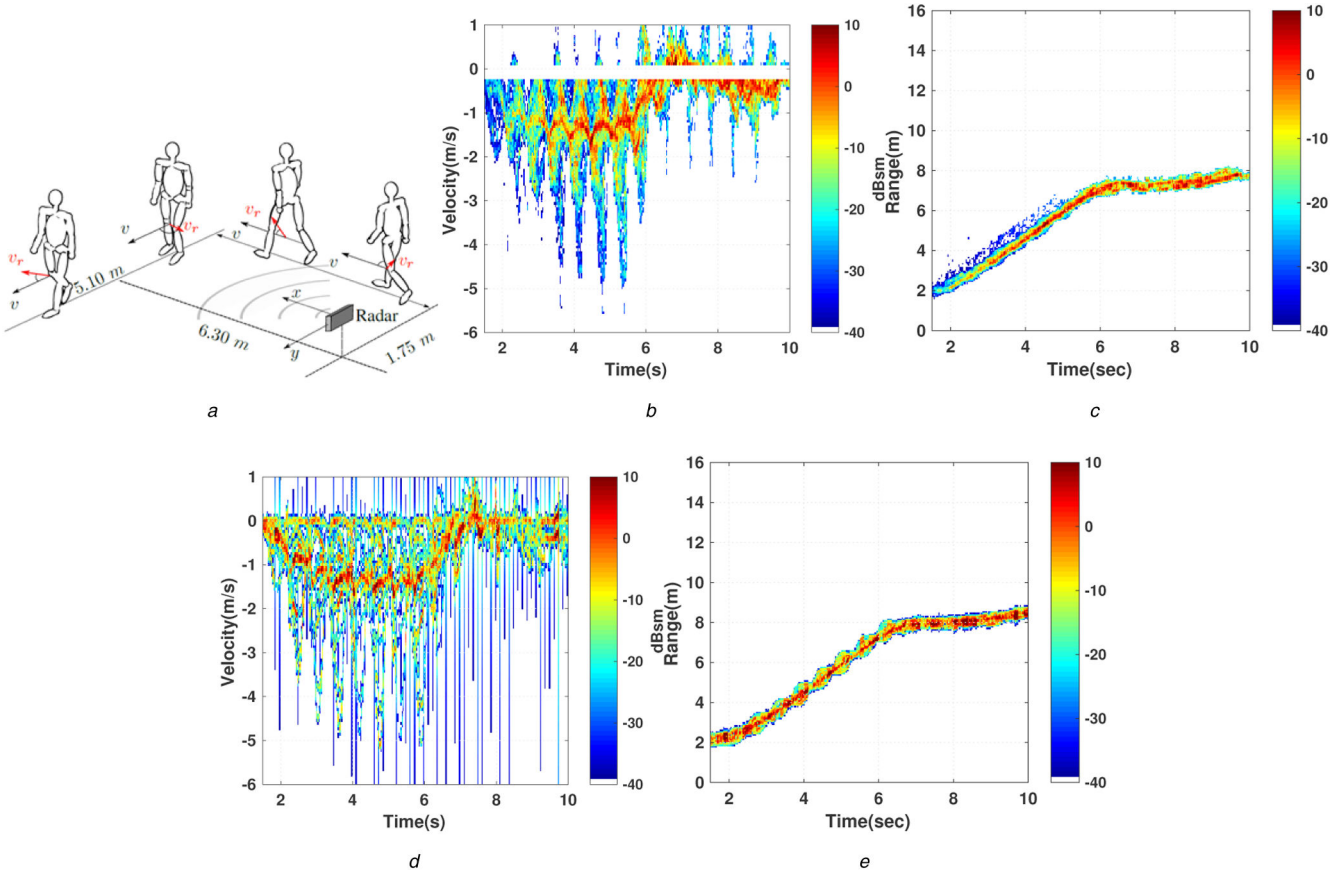

Fig. 11 *Radar signatures of a human walking away from the 77 GHz monostatic radar with perpendicular and tangential trajectory*
(a) Trajectory of a human walking away from the radar and then turning and walking tangentially across it, ***(b)*** Measured Doppler-time spectrogram, ***(c)*** Measured range-time spectrogram, ***(d)*** Simulated Doppler-time spectrogram, ***(e)*** Simulated range-time spectrogram from measurement data

Table 4 Quantitative comparison between simulated and measured range-time, Doppler time and range–Doppler plots for second target trajectory

Algorithm	Metric	Range versus time	Doppler versus time
proposed	SSIM	0.87	0.71
proposed	NMSE	0.13	0.13
proposed	NCC	0.98	0.97
proposed	MI	0.13	0.11

Dopplers due to the different limbs. Then when the subject moves tangentially across the radar, the Doppler values are quite low. Further, a notch filter is implemented across the DC bin to remove static clutter in the measurement result. In the range-time measurement results in Fig. 11*c*, the range of the target increases with time and then remains fairly constant while the subject walks tangentially across the field-of-view of the radar. In both of the measurement results, the strongest returns arise from the torso while the weaker returns arise from the arms and legs.

The simulation results for Doppler-time and range-time signatures are shown in Figs. 11*d* and *e,* respectively. Note that visually, there is a very good qualitative agreement between the simulated and measured results. The proposed technique correctly estimates the span of the RCS values of humans. However, there is a key difference in the signatures – the presence of additional spikes in the Doppler-time spectrograms. These are caused by time discontinuities in the MoCap data especially during the human turning motion (a well-known limitation of MoCap technology). These are not caused by any artefact from the proposed simulation process. Quantitative metrics (NMSE, SSIM, MI and NCC) shown in Table 4, indicate that there is good agreement between the measured and simulated results. Due to the aforementioned spikes (during target undertaking turns) in the simulation results, the results are slightly poorer than the previous case where the target walked along a straight line.

The computational complexity of the proposed approach required ray tracing to be carried out at video frame rate, matrix inversion operations for determining scattering coefficients and linear operations for point scatterer modelling at radar sampling frequencies. The matrix inversion operation is computationally not very hard due to the small size of the matrix ($[(K \simeq B) \times B]$). Among these three steps, the ray-tracing operation is the most computationally expensive and hence we discuss its complexity in the Appendix. If the same human subject is considered, then the scattering coefficients $a_b, b = 1{:}B$ computed across 1 T_{long} duration can be reused without a significant increase in the error. This has been tested for the two trajectories of the humans reported in this paper. The results were almost identical to those reported in Tables 3 and 4.

4 Conclusion

The shooting and bouncing ray technique based on ray tracing and geometric optics have been used extensively to accurately model the RCS of targets at high carrier frequencies. However, the technique is computationally extensive and hence not suitable for modelling the time-varying RCS of dynamic human motions, at radar sampling frequencies, since humans are spatially large 3D dielectric bodies with considerable variation in posture and pose. A computationally simpler alternative for modelling radar signatures of human motion is based on the scattering centre model. However,

the reflectivities of the scattering centres, in prior works, have been loosely approximated by RCS values of primitives resembling body shapes resulting in inaccurate estimates of RCS magnitudes.

In our work, we hypothesise that the scattering coefficients fluctuate very slowly over multiple CPIs while the positions of the scatterers change rapidly across multiple PRIs. Therefore, we estimate the scattering centre coefficients by combining the point scatterer model with the ray tracing RCS estimates in a linear regression framework. The positions of the scattering centres are obtained from an animation model of a pedestrian gathered from MoCap data. We use the reflectivity estimates to obtain realistic radar scattered signal that is processed to obtain commonly used radar signatures such as range–time, Doppler–time and range–Doppler ambiguity plots. Simultaneous to the MoCap data collection, we gathered measurement data using an automotive radar at 77 GHz from which the radar signatures were generated. The proposed simulated signatures showed a low-normalised mean square error (<10%) and high structural similarity (>80%) with respect to the measured signatures. We compared the proposed simulation signatures with simulation results of state-of-art primitive-based modelling to indicate the efficacy of the proposed method. We also demonstrated the versatility of our simulation method for modelling radar signatures at different polarisations, aspect angles and carrier frequencies.

5 References

[1] WHO: 'Global status report on road safety 2018 (2018)', 2019, https://www.who.int/violence_injury_prevention/road_safety_status/2018/English-Summary-GSRRS2018.pdf

[2] NHTSA: 'Traffic safety facts 2017 data: pedestrians'. Available at https://crashstats.nhtsa.dot.gov/Api/Public/ViewPublication/81268, retrieved March 2019

[3] Schiele, B., Wojek, C.: 'Camera based pedestrian detection', in Winner, H., Hakuli, S., Lotz, F., *et al.* (Eds.): '*Handbook of driver assistance systems: basic information, components and systems for active safety and comfort*' (Springer, Germany, 2016), pp. 525–545

[4] Ragesh, N., Rajesh, R.: 'Pedestrian detection in automotive safety: understanding state-of-the-art', *IEEE Access*, 2019, **7**, pp. 47864–47890

[5] Severino, J.V.B., Zimmer, A., dos Santos Coelho, L., *et al.*: 'Radar based pedestrian detection using support vector machine and the micro Doppler effect'. European Symp. on Artificial Neural Networks, Computational Intelligence and Machine Learning, Bruges, Belgium, 2018

[6] Majer, F., Yan, Z., Broughton, G., *et al.*: 'Learning to see through haze: radar-based human detection for adverse weather conditions'. 2019 European Conf. on Mobile Robots (ECMR), Prague, Czech Republic, 2019, pp. 1–7

[7] Held, P., Steinhauser, D., Kamann, A., *et al.*: 'Radar-based analysis of pedestrian micro-Doppler signatures using motion capture sensors'. 2018 IEEE Intelligent Vehicles Symp. (IV), Changshu, China, 2018, pp. 787–793

[8] Steinhauser, D., Held, P., Kamann, A., *et al.*: 'Micro-Doppler extraction of pedestrian limbs for high resolution automotive radar'. 2019 IEEE Intelligent Vehicles Symp. (IV), Paris, France, 2019, pp. 764–769

[9] Fairchild, D.P., Narayanan, R.M.: 'Classification of human motions using empirical mode decomposition of human micro-Doppler signatures', *IET Radar Sonar Navig.*, 2014, **8**, (5), pp. 425–434

[10] Stolz, M., Schubert, E., Meinl, F., *et al.*: 'Multi-target reflection point model of cyclists for automotive radar'. 2017 European Radar Conf. (EURAD), Nuremburg, Germany, 2017, pp. 94–97

[11] Angelov, A., Robertson, A., Murray-Smith, R., *et al.*: 'Practical classification of different moving targets using automotive radar and deep neural networks', *IET Radar Sonar Navig.*, 2018, **12**, (10), pp. 1082–1089

[12] Prophet, R., Hoffmann, M., Ossowska, A., *et al.*: 'Pedestrian classification for 79 GHz automotive radar systems'. 2018 IEEE Intelligent Vehicles Symp. (IV), Changshu, China, 2018, pp. 1265–1270

[13] Duggal, G., Ram, S.S., Mishra, K.V.: 'Micro-Doppler and Micro-range detection via Doppler-resilient 802.11 ad-based vehicle-to-pedestrian radar'. 2019 IEEE Radar Conf. (RadarConf), 2019

[14] Du, R., Fan, Y., Wang, J.: 'Pedestrian and bicyclist identification through micro Doppler signature with different approaching aspect angles', *IEEE Sens. J.*, 2018, **18**, (9), pp. 3827–3835

[15] Ram, S.S., Gurbuz, S.Z., Chen, V.C.: 'Modeling and simulation of human motions for micro-Doppler signatures', in Amin, M. (Ed.): '*Radar for indoor monitoring*' (CRC Press, Boca Raton, FL, USA, 2017), pp. 39–69

[16] Park, J., Johnson, J.T., Majurec, N., *et al.*: 'Simulation and analysis of polarimetric radar signatures of human gaits', *IEEE Trans. Aerosp. Electron. Syst.*, 2014, **50**, (3), pp. 2164–2175

[17] Khomchuk, P., Stainvas, I., Bilik, I.: 'Pedestrian motion direction estimation using simulated automotive MIMO radar', *IEEE Trans. Aerosp. Electron. Syst.*, 2016, **52**, (3), pp. 1132–1145

[18] Smith, G.E., Woodbridge, K., Baker, C.J.: 'Multistatic micro-Doppler signature of personnel'. 2008 IEEE Radar Conf. RADAR'08, Rome, Italy, 2008, pp. 1–6

[19] Tsai, Y.Y., Lin, W.C., Cheng, K.B., *et al.*: 'Real-time physics-based 3D biped character animation using an inverted pendulum model', *IEEE Trans. Vis. Comput. Graphics*, 2010, **16**, (2), pp. 325–337

[20] Boulic, R., Thalmann, N.M., Thalmann, D.: 'A global human walking model with real-time kinematic personification', *Vis. Comput.*, 1990, **6**, (6), pp. 344–358

[21] Ram, S.S., Ling, H.: 'Simulation of human micro Dopplers using computer animation data'. 2008 IEEE Radar Conf. RADAR'08, Rome, Italy, 2008, pp. 1–6

[22] Ram, S.S., Ling, H.: 'Micro Doppler signature simulation of computer animated human and animal motions'. 2008 IEEE Antennas and Propagation Society Int. Symp. AP-S 2008, San Diego, CA, USA, 2008, pp. 1–4

[23] Erol, B., Gurbuz, S.Z.: 'A kinect-based human micro-Doppler simulator', *IEEE Aerosp. Electron. Syst. Mag.*, 2015, **30**, (5), pp. 6–17

[24] Software, S.M. (Ed.) 'Poser', Smith Micro Software, 2019. Available at http://my.smithmicro.com/poser-3d-animation-software.html

[25] Chattopadhyay, S., Bhandarkar, S.M., Li, K.: 'Human motion capture data compression by model-based indexing: a power aware approach', *IEEE Trans. Vis. Comput. Graphics*, 2007, **13**, (1), pp. 5–14

[26] Dogaru, T., Nguyen, L., Le, C.: '*Computer models of the human body signature for sensing through the wall radar applications*' (Army Research Lab, Adelphi, 2007)

[27] Dogaru, T., Le, C.: '*Validation of Xpatch computer models for human body radar signature*' (Army Research Lab, Adelphi, 2008)

[28] Le, C., Dogaru, T.: '*Numerical modeling of the airborne radar signature of dismount personnel in the UHF-, L-, Ku-, and Ka-bands*' (Army Research Lab, Adelphi, 2007)

[29] van Dorp, P., Groen, F.: 'Human walking estimation with radar', *IEE Proc., Radar Sonar Navig.*, 2003, **150**, (5), pp. 356–365

[30] Ram, S.S., Christianson, C., Kim, Y., *et al.*: 'Simulation and analysis of human micro-Dopplers in through-wall environments', *IEEE Trans. Geosci. Remote Sens.*, 2010, **48**, (4), pp. 2015–2023

[31] Erol, B., Gurbuz, S.Z., Amin, M.G.: 'GAN-based synthetic radar micro-Doppler augmentations for improved human activity recognition'. 2019 IEEE Radar Conf. (RadarConf), Boston, MA, USA, 2019, pp. 1–5

[32] Alnujaim, I., Oh, D., Kim, Y.: 'Generative adversarial networks to augment micro-Doppler signatures for the classification of human activity'. IGARSS 2019-2019 IEEE Int. Geoscience and Remote Sensing Symp., Yokohama, Japan, 2019, pp. 9459–9461

[33] Garcia-Fernandez, A.F., Yeste-Ojeda, O.A., Grajal, J.: 'Facet model of moving targets for ISAR imaging and radar back-scattering simulation', *IEEE Trans. Aerosp. Electron. Syst.*, 2010, **46**, (3), pp. 1455–1467

[34] Ling, H., Chou, R.C., Lee, S.W.: 'Shooting and bouncing rays: calculating the RCS of an arbitrarily shaped cavity', *IEEE Trans. Antennas Propag.*, 1989, **37**, (2), pp. 194–205

[35] Chen, M., Chen, C.C., Chien, S.Y.P., *et al.*: 'Artificial skin for 76–77 GHz radar mannequins', *IEEE Trans. Antennas Propag.*, 2014, **62**, (11), pp. 5671–5679

[36] Williams, G.: 'Overdetermined systems of linear equations', *Am. Math. Mon.*, 1990, **97**, (6), pp. 511–513

[37] Schepers, M., Giuberti, M., Bellusci, G., *et al.* (Eds.): 'Xsens MVN: consistent tracking of human motion using inertial sensing', Xsens, 2018. Available at https://www.xsens.com/functions/inertial-sensor-modules/

[38] INRAS (Ed.): 'Radarlog product description', INRAS. Available at http://www.inras.at/en/products/new-radarlog.html

[39] Yamada, N., Tanaka, Y., Nishikawa, K.: 'Radar cross section for pedestrian in 76 GHz band'. 2005 European Microwave Conf., Paris, France, 2005, vol. 2, pp. 4

[40] Amin, M.G.: '*Through-the-wall radar imaging*' (CRC press, Boca Raton, FL, USA, 2017)

[41] Ruck, G.T., Barrick, D.E., Stuart, W.D., *et al.*: '*Radar cross section handbook*', vol. **1** (Plenum Press, New York, 1970)

[42] Ludloff, A.K.: '*Praxiswissen radar und radarsignalverarbeitung*' (Springer-Verlag, Germany, 2013)

[43] Wang, Z., Bovik, A.C., Sheikh, H.R., *et al.*: 'Image quality assessment: from error visibility to structural similarity', *IEEE Trans. Image Process.*, 2004, **13**, (4), pp. 600–612

[44] Wenger, J.: 'Automotive radar-status and perspectives'. IEEE Compound Semiconductor Integrated Circuit Symp., 2005. CSIC'05, Palm Springs, CA, USA, 2005, pp. 4–pp

[45] Rubin, S.M., Whitted, T.: 'A 3-dimensional representation for fast rendering of complex scenes'. ACM SIGGRAPH Computer Graphics, Seattle, WA, USA, 1980, vol. 14, pp. 110–116

[46] Fujimoto, A., Iwata, K.: 'Accelerated ray tracing', in Kunii, T.L. (Ed.): '*Computer graphics*' (Springer, Tokyo, Japan, 1985), pp. 41–65

6 Appendix

6.1 Pedestrian RCS at alternate radar configurations

The second popular band of carrier frequencies for automotive radar is 24 GHz [44]. We present the monostatic RCS for different polarisations and incident angles in Fig. 12. The figure shows that the RCS values are slightly higher for the horizontal co-polarisation scenario when compared to the vertical polarisation especially for the case of frontal incidence (0°). On average, the frontal incidence also gives rise to the highest RCS values for the monostatic configuration. In some *V2X* applications, it may be useful to have bistatic RCS of pedestrians. Figs. 13 and 14, present

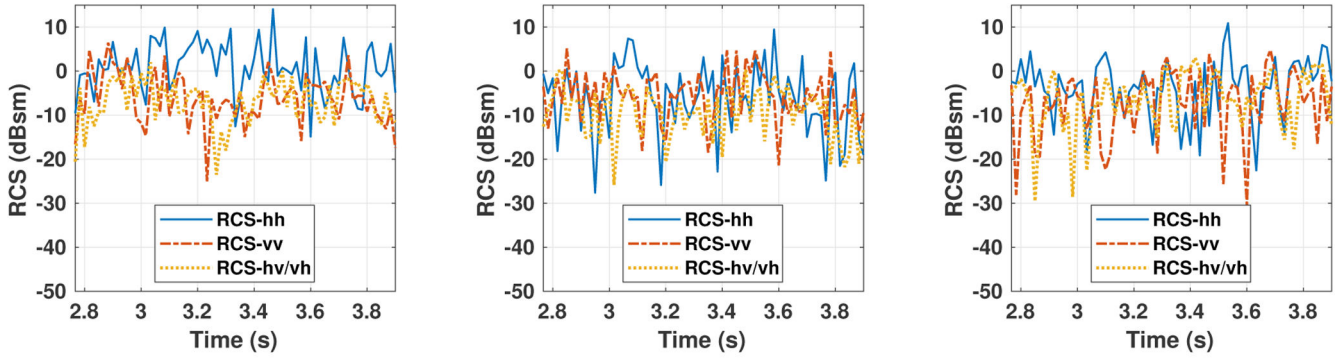

Fig. 12 *Simulated monostatic ($\phi^i = \phi^s$) RCS across multiple frames corresponding to one walking stride obtained from ray tracing at 24 GHz for three aspect angles*

(a) Front incidence ($\phi^i = 0°$), ***(b)*** Oblique incidence ($\phi^i = 45°$), ***(c)*** 90° incidence ($\phi^i = 90°$)

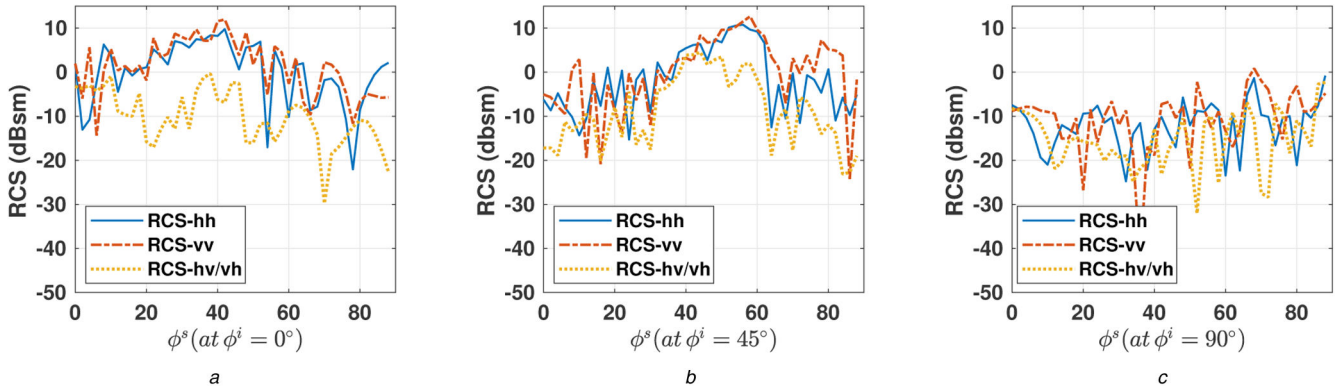

Fig. 13 *Simulated bistatic RCS versus ϕ^s such that bistatic aspect angle = $\phi^s - \phi^i$; for single frame/pose for three aspect angles*

(a) Front incidence ($\phi^i = 0°$), ***(b)*** oblique incidence ($\phi^i = 45°$), ***(c)*** 90° incidence ($\phi^i = 90°$) at 77 GHz

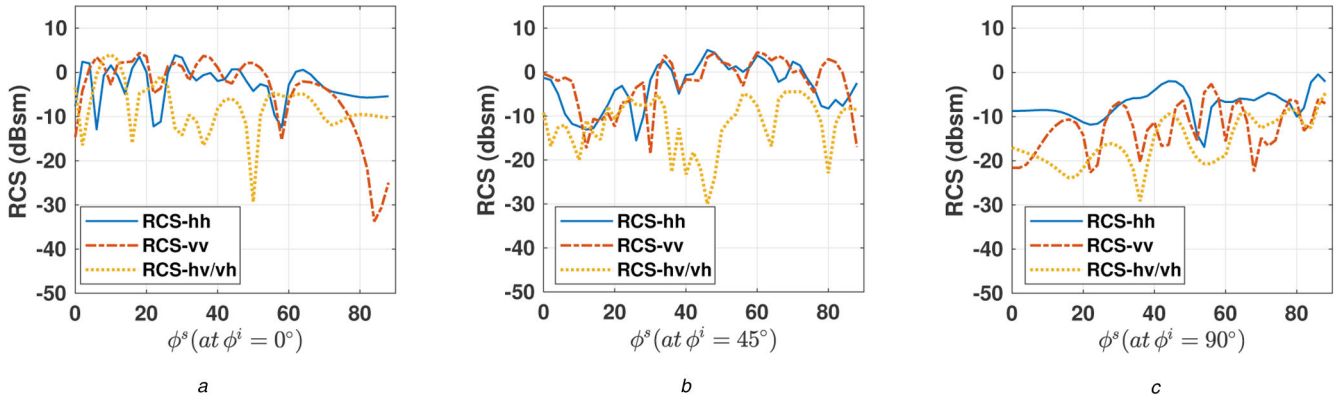

Fig. 14 *Simulated bistatic RCS versus ϕ^s such that bistatic aspect angle = $\phi^s - \phi^i$; for single frame/pose for three aspect angles*

(a) Front incidence ($\phi^i = 0°$), ***(b)*** Oblique incidence ($\phi^i = 45°$), ***(c)*** 90° incidence ($\phi^i = 90°$) at 24 GHz

the variation of RCS with ϕ^s for bistatic angle $= \phi^s - \phi^i$; for a single frame/pose for different polarisations and for three different incident angles for two automotive frequencies 24 and 77 GHz. The bistatic RCS corresponds to the monostatic RCS when $\phi^s = \phi^i$. Interesting, the bistatic RCS is higher than the monostatic RCS at some aspect angles for some postures of the human.

6.2 Computational complexity of the proposed approach

In Fig. 15, we indicate the computational time for generating the results for different processing configurations. A realistic model of the human requires the body to be rendered by a large number of small sized triangular facets. For ray tracing, we consider a large volume of parallel illumination rays emanating from an illumination plane from grid points that must be densely placed at least $\lambda/10$ apart. The computational complexity is determined by the intersection tests between all the illumination rays and the facets on the body. This results in considerable complexity (800 min to compute RCS at 77 GHz in Fig. 15). Several works in graphics have addressed the challenges of reducing the computational complexity associated with ray tracing [45, 46]. We have implemented the bounding box test in our work where the poly-mesh human is divided into several distinct parts each enclosed by a spatial bounding box. Instead of testing every ray with every triangle, we test every ray with every bounding box. Only if the ray intersects the bounding box, do we test the intersection of the ray with every facet within the bounding box. By using bounding box technique on a single core processor, we observed about 14 times reduction in computation time from 800 to 60 min in Fig. 15. Since the ray-triangle intersection tests can be carried out in parallel, the computation time can be further reduced by implementing the algorithm across multiple parallel processors. The algorithm was implemented using the parallel computing tool

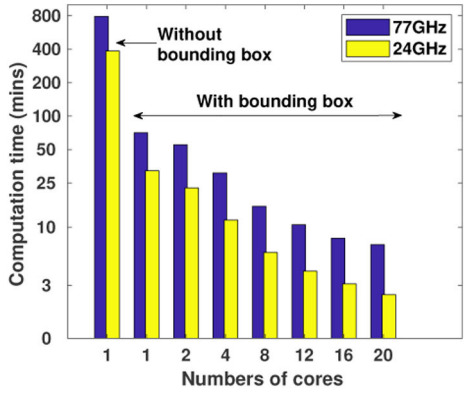

Fig. 15 *Reduction in computation time of RCS using electromagnetic ray tracing, with the introduction of bounding box technique and increasing the number of cores for parallel processing at 77 and 24 GHz*

box of Matlab. By using the parallel processing with the bounding box technique, the computation time was further reduced to 8 min for a 20 core system.